2020

Strain rate dependent failure criteria for fibrous composites using multiscale approach

Kwon, Y.W.; Panick, C.J.

Springer

Kwon, Y. W., and C. J. Panick. "Strain rate dependent failure criteria for fibrous composites using multiscale approach." Multiscale and Multidisciplinary Modeling, Experiments and Design 3.1 (2020): 11-22.
http://hdl.handle.net/10945/65688

Multiscale and Multidisciplinary Modeling, Experiments and Design (2020) 3:11–22
https://doi.org/10.1007/s41939-019-00055-0

ORIGINAL PAPER

Strain rate dependent failure criteria for fibrous composites using multiscale approach

Y. W. Kwon[1] · **C. J. Panick**[1]

Received: 7 June 2019 / Accepted: 20 July 2019 / Published online: 3 August 2019

Abstract
Recently, a set of failure criteria based on a multiscale model was developed for fibrous composites. Those criteria used stresses and strains occurring in the fiber and matrix material level. The failure criteria consisted of three failure modes such as fiber failure, matrix failure, and fiber/matrix interface failure. Those criteria were developed for quasi-static loading such that the effect of the strain rate was not under consideration. To model and predict failure of composite materials and structures subjected to dynamic loading, the effect of strain rate needs to be included in the failure criteria. The present work is to revise the former criteria to be applicable to the strain rate dependent composite materials, especially polymer composites. To validate the revised failure criteria, Charpy impact testing as well as quasi-static uniaxial testing were conducted. The test results agreed well with predicted failure loads using the new failure criteria.

Keywords Failure criteria · Fibrous composite material · Strain rate effect · Multiscale analysis · Polymer composite

1 Introduction

Fibrous composite materials have been used for various engineering applications and their usage has increased steadily because of the beneficial properties. This trend is expected to continue in the future. As composite materials are used for load-bearing components, it is important to predict the failure load of those components to prevent them from failure. To do that, reliable failure criteria are needed for engineering design and analysis of load-carrying composite structures.

Unlike metallic materials, fibrous composites have complex failure modes and mechanisms. Many failure criteria have been proposed in the past (Hinton et al. 2004; Tsai and Wu 1971; Hashin 1980; Sun et al. 1996; Hütter et al. 1974; Swanson et al. 1987; Kwon and Darcy 2018a, b). The failure criteria can be classified into two major groups. One group of failure criteria considers failures at the lamina level-like a single layer of fibrous composite made of continuous fibers and the binding matrix. For this group, laminar specimens are tested under different loading conditions to determine the necessary parameters that are required for the respective failure criteria.

Some failure criteria for fibrous composite materials used a single equation that does not necessarily distinguish one failure mode from another explicitly. Different failure modes are included in one equation. Depending on the loading condition, failures associated with one mode or combined modes are represented by a single equation. For example, the biquadratic failure criterion called the Tsai-Wu (1971) criterion is one of the examples. Other failure criteria have multiple failure equations depending on the failure mode such as fiber failure, matrix failure, etc. The failure criterion proposed by Hashin (1980) is an example for this kind of failure criteria.

Another group of failure criteria considered failures of the fiber and matrix material individually as well as the fiber/matrix interface failure. This kind of criteria requires the stress and strain information at the fiber and matrix materials, respectively, as well as at their interface. To find the stress and strain at the constituent material level, a multiscale approach should be utilized. The criterion proposed by Kwon and Darcy (2018a, b) is an example. To make the multiscale approach practical for usage, the technique should be computationally efficient. To this end, the multiscale approach used analytical solutions in conjunction with structural finite

✉ Y. W. Kwon
ywkwon@nps.edu

[1] Department of Mechanical and Aerospace Engineering, Naval Postgraduate School, Monterey, CA 93943, USA

element analysis. Therefore, the computational cost is very minimum to apply the multiscale failure criteria.

All failure criteria were initially developed without considering strain rate effects. Later more research was undertaken to study the effect of strain rate on polymer composites and to develop failure criteria including the strain rate effect (Daniel et al. 2011; Hsiao and Daniel 1998; Sierakowski 1997; Jacob et al. 2004). The present work is to extend the failure criteria based on the multiscale approach to include the strain rate effect because many dynamic loading conditions induce strain rates in composite structures. Therefore, it is necessary to have failure criteria that can include the effect of strain rate in predicting failure of fibrous composite materials.

This paper describes the proposed failure criteria in the next section. The following section discusses a set of physical experiments conducted to validate the proposed criteria. Then numerical modeling is discussed to predict the failure using the proposed failure criteria. Finally, experimental results and numerical comparisons are provided later for the strain rates from quasi-static up to about 300 s^{-1}, which are followed by conclusions.

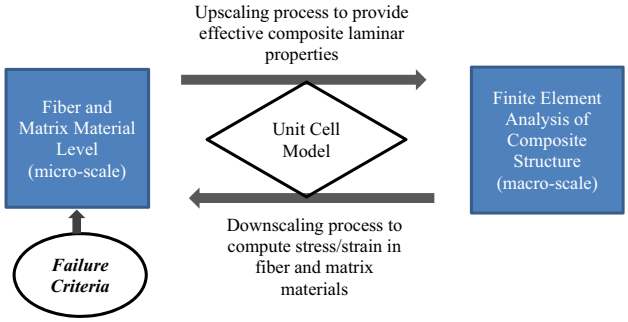

Fig. 1 Sketch of multiscale analysis of laminated fibrous composites

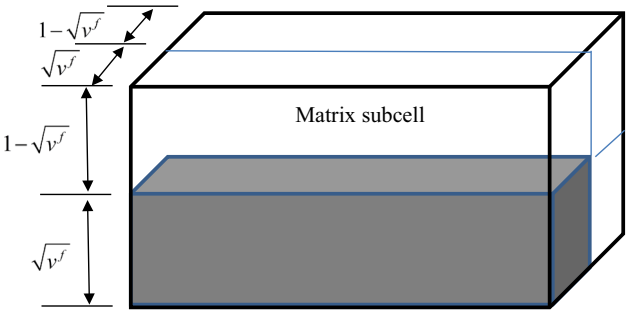

Fig. 2 Unit-cell model made of one fiber subcell and three matrix subcell

2 Failure criteria

The recently proposed failure criteria for continuous fiber composites considered failure modes in terms of the constituent materials. As a result, the failure modes were fiber failure, matrix failure, and fiber/matrix interface failure. Most of the fibers are brittle, and fiber failure is usually different depending on tensile and compressive loading. Fibers break under tension and may buckle under compression. Matrix failure depends on the matrix material. If the matrix material is resin or epoxy, brittle failure modes are more common. In such cases, the maximum strain criterion is a good choice for the material. Failure of the fiber/matrix interface depends on the interface strength and the stresses at the interface. Both shear stress and peeling stress at the interface are important to determine the failure.

To apply those failure criteria at the constituent material level, it is necessary to obtain the stresses and strains occurring in the fiber and matrix as well as at their interface. To find those values, a multiscale approach was applied. Figure 1 sketches the multiscale analysis loop for a typical laminated composite structure made of continuous fibers. The multiscale analysis loop has two phases. The first phase is an upscaling process while the second phase is a downscaling process. The upscaling process is also called the stiffness phase, while the downscaling process is called the strength phase.

The upscaling process computes the effective material properties of the larger length scale from the material properties of the smaller length scale. In this application, the effective composite material properties of a laminar are computed from the fiber and matrix material properties and their volume fractions. That is why the upscaling process is also called the stiffness phase. On the other hand, the downscaling process decomposes the stresses and strains of the larger length scale into those at the smaller length scale. The stresses and strains in the fiber and matrix level are computed from those at a laminar level.

To undertake both upscaling and downscaling processes, an analytical unit-cell model was developed. Therefore, the overall computational cost is minimized even though so many iterations are required for each analysis. The geometric sketch of the unit-cell model is shown in Fig. 2. The unit-cell consists of subcells. There are four subcells for the continuous fiber composite. One subcell represents the fiber and the others are for the matrix material. The subcell sizes are dependent on the fiber and matrix volume fraction. If there are voids in the composite materials, the voids can also be included in the model. However, a no-void condition was assumed in the present analysis.

The details of the unit-cell model were presented in Kwon and Darcy (2018a, b), Kwon and Kim (1998), Kwon and Park (2013), Kwon et al. (2016), Park and Kwon (2013) and Kwon (2016). Therefore, they are not repeated for simplicity. Instead, a brief summary of the model is presented. Every subcell is assumed to have a uniform state of stress and strain. Then, stress equilibriums at the interface between any two

subcells are applied. Deformation compatibilities are also applied using subcell strains. In addition, every subcell has its own constitutive relationship between stresses and strains. Finally, the unit-cell (i.e. composite) level stresses and strains are assumed equivalent to the volumetric sums of subcell stresses and strains. Solving those equations provides the mathematical expressions necessary for the upscaling and downscaling processes.

For the upscaling process, the following expression is used.

$$E^{\mathrm{u}}_{ijkl} = f(E^{\mathrm{s}}_{ijkl}, v^{\mathrm{f}}, v^{\mathrm{m}}) \tag{1}$$

where E^{u}_{ijkl}, and E^{s}_{ijkl} are the material property tensors for the unit cell and subcells, respectively, and v is the volume fraction, while superscripts 'f' and 'm' denote the fiber and matrix materials. If there are no voids, $v^{\mathrm{f}} + v^{\mathrm{m}} = 1$. Likewise, the following expression is utilized for the downscaling process.

$$\varepsilon^{\mathrm{s}}_{ij} = g(\varepsilon^{\mathrm{u}}_{ij}, v^{\mathrm{f}}, v^{\mathrm{m}}) \tag{2}$$

in which $\varepsilon^{\mathrm{s}}_{ij}$ and $\varepsilon^{\mathrm{u}}_{ij}$ are the strain tensors at the subcell and unit cell, respectively. Then, the subcell stresses are computed from the subcell strains using their constitutive equations.

Once the subcell (i.e. fiber and matrix level) stresses and strains are determined, failure criteria are applied to the stresses and/or strains to determine failure. The failure criterion for the polymer fiber was based on the fiber strains such as,

$$\begin{cases} \left(\varepsilon^{\mathrm{f}}_{xx}\right)^2 + \left(2\varepsilon^{\mathrm{f}}_{xy}\right)^2 + \left(2\varepsilon^{\mathrm{f}}_{xz}\right)^2 \geq \left(\varepsilon^{\mathrm{f}}_{\mathrm{ten}}\right)^2 & \text{if } \varepsilon^{\mathrm{f}}_{xx} > 0 \\ \left(\varepsilon^{\mathrm{f}}_{xx}\right)^2 + \left(2\varepsilon^{\mathrm{f}}_{xy}\right)^2 + \left(2\varepsilon^{\mathrm{f}}_{xz}\right)^2 \geq \left(\varepsilon^{\mathrm{f}}_{\mathrm{comp}}\right)^2 & \text{if } \varepsilon^{\mathrm{f}}_{xx} < 0 \end{cases} \tag{3}$$

where the superscript 'f' indicates the fiber material, the x axis is the direction of the fiber orientation, and the $\varepsilon^{\mathrm{f}}_{\mathrm{ten}}$ and $\varepsilon^{\mathrm{f}}_{\mathrm{comp}}$ are the tensile and compressive failure strains of the fiber material, respectively. In other words, the fiber failure strain may be different depending on tensile or compressive loading.

The failure criterion for the resin or epoxy matrix used the maximum strain criterion. That is, when the principal strains of the matrix material are equal to or greater than the failure strain of the material in either tension or compression in terms of magnitude, the matrix was considered to fail, as stated in Eq. (4):

$$\varepsilon^{\mathrm{m}}_1 \geq \varepsilon^{\mathrm{m}}_{\mathrm{ten}} \text{ or } \varepsilon^{\mathrm{m}}_3 \leq \varepsilon^{\mathrm{m}}_{\mathrm{comp}} \tag{4}$$

where the superscript 'm' denotes the matrix material, subscripts '1' and '3' are the largest and the smallest principal strains, and $\varepsilon^{\mathrm{m}}_{\mathrm{ten}}$ and $\varepsilon^{\mathrm{m}}_{\mathrm{comp}}$ are the failure strain of the matrix in tension and compression, respectively.

The fiber/matrix interface failure is more complex than the other two criteria. The proposed failure criterion in the xy-plane was,

$$\left(\frac{\tau^{\mathrm{int}}_{xy} + \sqrt{v^{\mathrm{f}}}\left(\sigma^{\mathrm{m}}_{yy} - \sigma^{\mathrm{m}}_{xx}\right)}{\tau^{\mathrm{int}}_{\mathrm{fail}}}\right)^2 + \mu\left(\frac{\sigma^{\mathrm{m}}_{yy}}{\sigma^{\mathrm{int}}_{\mathrm{fail}}}\right) \geq 1 \tag{5}$$

Here τ^{int}_{xy} and $\tau^{\mathrm{int}}_{\mathrm{fail}}$ are the fiber/matrix interface shear stress and the failure strength under pure shear loading. In addition, $\sigma^{\mathrm{int}}_{\mathrm{fail}}$ is the interface failure strength under pure peeling stress. Because the interface normal stress results in differing effects on the failure depending on its direction, μ is 1 if the interface normal stress is tensile, and zero otherwise.

Those criteria were developed for the quasi-static loading, i.e. independent of strain rates. Polymer composite materials show rate-dependent material properties, especially failure strength. Because the present failure criteria are based on the respective failure of the fiber and matrix material, the effect of strain rate can also be considered individually for the fiber and matrix materials.

A preliminary test showed that the polymer matrix material is much more sensitive to strain rate while the polymer fiber material is less dependent on strain rate. For this kind of composite material, the effect of strain rate is applied to the matrix material. Therefore, the matrix and interface failure strengths are modified based on the strain rate.

Two mathematical expressions have been used frequently to represent the strain rate effect on the strength of materials as given in Eqs. (6) and (7):

$$1 + \left(\frac{\dot{\varepsilon}}{D}\right)^{\frac{1}{p}} \tag{6}$$

and

$$\alpha \log_{10} \frac{\dot{\varepsilon}}{\dot{\varepsilon}_o} + 1 \tag{7}$$

Here $\dot{\varepsilon}$ is the strain rate applied to the material. Equation (6) has two material dependent constants p and D while Eq. (7) has the two constants α and $\dot{\varepsilon}_o$. By selecting proper constants for each equation, both expressions can provide very close values if the strain rate is greater than 1.0. The present study implemented Eq. (7) to modify the failure values for matrix and interface failures. In other words, the failure strain of the matrix material $\varepsilon^{\mathrm{m}}_{\mathrm{fail}}$ at the strain rate $\dot{\varepsilon}$ is expressed as

$$\varepsilon^{\mathrm{m}}_{\mathrm{fail}}(\dot{\varepsilon}) = \varepsilon^{\mathrm{m}}_{\mathrm{fail}}(\dot{\varepsilon}_o)\left[\alpha \log_{10} \frac{\dot{\varepsilon}}{\dot{\varepsilon}_o} + 1\right] \tag{8}$$

where $\varepsilon^{m}_{fail}(\dot{\varepsilon}_o)$ is the matrix failure strain at the quasi-static strain rate $\dot{\varepsilon}_o$.

Similarly, the strain rate modified the interface failure strength as shown in Eqs. (9) and (10):

$$\tau^{int}_{fail}(\dot{\varepsilon}) = \tau^{int}_{fail}(\dot{\varepsilon}_o)\left[\alpha\sqrt{3}\log_{10}\frac{\dot{\varepsilon}}{\dot{\varepsilon}_o} + 1\right] \tag{9}$$

and

$$\sigma^{int}_{fail}(\dot{\varepsilon}) = \sigma^{int}_{fail}(\dot{\varepsilon}_o)\left[\alpha\ \log_{10}\frac{\dot{\varepsilon}}{\dot{\varepsilon}_o} + 1\right] \tag{10}$$

3 Experimental procedure

Experiments were conducted for carbon fiber composites under quasi-static uniaxial loads as well as Charpy impact loads. The composite plates were unidirectional and symmetric cross-ply laminates whose thickness was 1.9 mm. Test samples were cut out of the laminated composite plates as shown in Table 1 for every type of specimen. Two kinds of test samples were prepared from each laminated plate, respectively. Specimens 'U1' and 'U2' have fibers along the longitudinal and transverse axis of the samples, respectively. Specimen 'B1' has fibers along the longitudinal direction in the most outer layers while specimen 'B2' has fibers along the transverse axis in the outer most layers.

Specimens for quasi-static and impact testing utilized different dimensions, but their thickness was the same. The quasi-static tensile test specimens had dimensions of 152.4 mm × 25.4 mm. At both ends of every tensile test samples, aluminum tabs were attached to prevent failure at the grip sites as sketched in Fig. 3. The tap had a 45° taper to avoid stress concentration. Omega SGD-7/350-LY11 strain gages were attached at the center of each sample along the longitudinal and transverse directions, respectively. The dimensions of the impact testing samples were 76.2 mm × 12.7 mm. One strain gage was affixed to the center of every impact sample along the longitudinal axis. The strain gage was on the tensile side because impact was applied to the compression side. No tap was utilized for the impact testing samples.

Quasi-static testing was performed using a uniaxial testing apparatus with a 2 mm/s extension rate. An Instron™ 100 kN tensile tester was utilized for tensile tests, which collected loads and displacements. The strain data were collected using a NI cDAQ-9174 system. Both data acquisition systems were synchronized so that all data points could be collected simultaneously. The load was applied until failure of each tensile sample. All samples failed at their mid-section as designed. Tensile tests were repeated at least twice for every kind of test specimen to check the consistency of the tests.

Table 1 Material properties of fiber and matrix material

Specimen name	Number of layers	Layer orientation
U1	6	0°/0°/0°/0°/0°/0°
U2	6	90°/90°/90°/90°/90°/90°
B1	6	0°/90°/0°/0°/90°/0°
B2	6	90°/0°/90°/90°/0°/90°

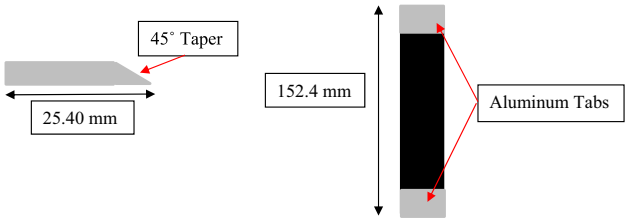

Fig. 3 Tensile test specimen

Strain rate tests were performed using a Tinius Olsen™ Charpy impact apparatus, and the strain gauge data were obtained via a high rate data acquisition system. It was initially determined that the strain rate tests were to be divided into three separate strain rates of increasing magnitude for each specimen layup and orientation. To accomplish this, the angle of the impact test hammer was varied to 20°, 45°, and 75°, respectively. These three impact angles resulted in the strain rates approximately 5 s^{-1} to 20 s^{-1} even though the rates varied more or less depending on the sample types. To achieve consistent impact hammer angles, a laser indicator was secured to a specified location on the impact hammer arm. The laser indicator was then projected onto a black grid placed directly behind the impact hammer arm. Simple geometric calculations were made to correlate the laser indicator height on the aforementioned grid with the angle of the impact hammer.

To collect a sufficiently large data set for each impact test sample, data acquisition rates such as 100 kHz and 500 kHz were used depending on the range of strain rates. A National Instruments™ (NI) PXIe-6358 data acquisition card was mounted to an NI PXIe-8821 chassis. The particular strain gauges used during impact and tensile testing required an excitation voltage of 10 V. Table 2 shows different kinds of impact specimens, the number of impact samples per specimen, the relevant data acquisition rates, and the impact hammer angles.

Because the Charpy impact test machine does not record the impact force-time history, a Honeywell™ Model 13 Subminiature Compression load cell was attached to the impactor in conjunction with the PXIe-6358 data acquisition card. To mount the load cell to the impactor, the load cell was attached to a steel sheath, and the impactor tip was inserted into the steel sheath and secured with a setscrew. Figure 4 shows the

Table 2 Impact test plan

Specimen name	# Samples tested	Data acquisition rate (Hz)	Impact hammer angles
U1	10	100 kHz or 300 kHz	20°, 45°, 75°
U2	10	100 kHz, 300 kHz, 400 kHz or 500 kHz	20°, 45°, 75°
B1	10	100 kHz or 300 kHz	20°, 45°, 75°
B2	10	100 kHz or 300 kHz	20°, 45°, 75

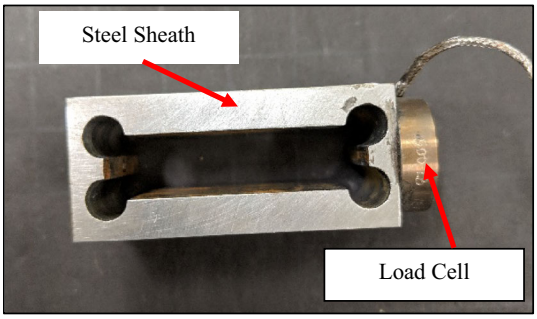

Fig. 4 Load cell attached to steel sheath

load cell affixed to a steel sheath. The load cell struck the composite samples directly.

4 Numerical modeling

Both tensile and impact specimens were modeled using eight-node solid elements using the UMAT of the ABAQUS finite element analysis program (Abaqus 6.13 User Manual 2015). The developed UMAT requires material properties of the fiber and matrix materials, respectively. Table 3 shows the material input for the quasi-static tensile model. The quasi-static specimen had 101,745 nodes and 85,200 elements in total, and each layer was modeled discretely while end tabs were not considered in the numerical model.

Due to the relative simplicity of the quasi-static finite element model, the boundary condition and loading condition were quite straightforward. One end of the long axis of the numerical model was constrained from any motion while a uniform displacement load was applied to the opposite side incrementally until failure.

The impact finite element model was also developed in accordance with material properties, geometries, and boundary conditions that most closely represented the experimental impact setup. Dynamic implicit analysis was undertaken for

Table 3 Material input to numerical analysis

Material property	Value
Longitudinal fiber elastic modulus (Pa)	220e+09 Pa
Transverse fiber elastic modulus (Pa)	28e+09 Pa
Fiber shear modulus, G_{12} (Pa)	30e+09 Pa
Fiber Poisson's ratio, ν_{12}	0.12
Fiber Poisson's ratio, ν_{23}	0.4
Matrix elastic modulus (Pa)	3e+09 Pa
Matrix shear modulus (Pa)	1.154e+09 Pa
Matrix Poisson's ratio	0.3
Volume fraction of fiber	0.5
Fiber tensile failure strain	0.0117
Fiber compressive failure strain	0.0117
Matrix tensile failure strain	0.0074
Matrix compressive failure strain	0.0074
Interface shear strength (Pa)	80e+06 Pa
Interface perpendicular strength (Pa)	54e+06 Pa

the impact specimen simulation with a time increment of 1 μs. The input material properties in the impact model were the same as those in Table 3 aside from the failure properties that were modified based on Eqs. (8)–(10) depending on the strain rate.

The element size of the impact model was the same as that of the quasi-static tension model. This resulted in 30,780 elements with 37,324 nodes. As before, each layer was modeled individually. The loading and boundary conditions of the impact model are more complicated than the tensile model. Figure 5 illustrates the boundary conditions applied to the impact model. The impact specimen was placed against rigid blocks. Therefore, contact boundary conditions were applied between the specimen and rigid blocks. The bottom side of the specimen was constrained along the vertical motion axis, and it was allowed rotation along the vertical axis. The center line of the specimen was allowed to move only in the transverse direction. Impact loads were applied to the mid-section of each sample, and the force–time histories obtained from the impact testing were used as the external loading to the model in a tabular form of force versus time.

5 Experimental results

First, the experimental results of the quasi-static tensile tests are presented for all specimens. Two samples of each case were quite consistent. Therefore, only one test result in each case was plotted. Figure 6 shows the stress–strain curves for specimens U1 and U2. As expected, specimen U1 is much stiffer and stronger than specimen U2. Both specimens showed brittle failures suggesting both fiber and matrix

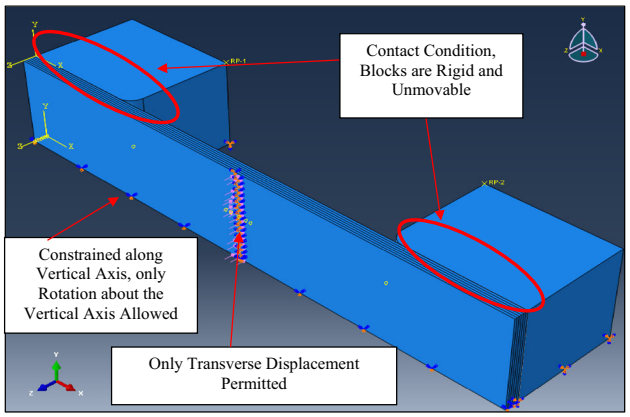

Fig. 5 Boundary condition applied to impact specimen model

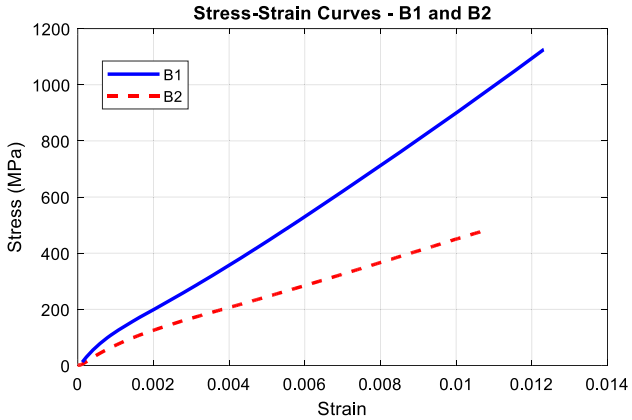

Fig. 7 Stress–strain curves for specimens B1 and B2

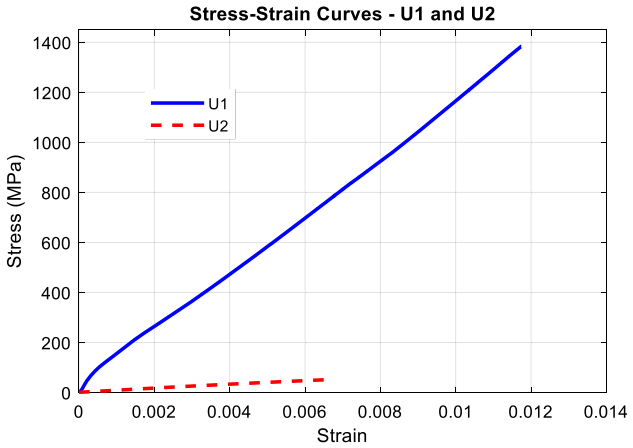

Fig. 6 Stress–strain curves for specimens U1 and U2

materials behaved in brittle matter. The graphs provide both stiffness and strength data of the unidirectional composite. Furthermore, the graphs show some strength information of the fiber and matrix materials. For example, the failure strain of the fiber material can be determined from the specimen U1 stress–strain curve because the fibers are the load-carrying element along that direction. For the specimen U2, the failure can be caused by either of the matrix failure and fiber/matrix interface failure. This can be observed by examining the fracture surface using a microscope.

The bidirectional specimens B1 and B2 were subject to the same loading rate as the unidirectional specimens, at 2 mm/s. The tensile specimen B2 had initial outer layer failure because these were the 90° layers. Figure 7 plots the stress–strain curves for the specimens B1 and B2. As Expected, specimen B1 is stiffer than specimen B2 because the former has more 0° layers than the latter.

The specimen U1 was also tested using the Charpy impact machine. Figure 8 displays the strains with respect to time for the three different initial angles, 20°, 45°, and 75°. Plotted data were cutoff at the point just before the failure of the sample. The strain gage reading showed unreasonably high strain when the specimen broke. The results of specimen U1 produced linear curves up to failure with varying strain rates depending on the impact hammer angles. The failure strains varied between 0.0115 and 0.0135 m/m. The different strain rates are easily observable in Fig. 8 based on the slopes of each strain versus time curve. As seen in the figure, the repeated tests for each impact case gave very consistent results. Therefore, the most representative graph was used in subsequent plots to simplify the graph unless otherwise mentioned. Strain rates were determined by applying a linear curve fit to each data set. The results did not show any trend of the failure strain as a function of the strain rate. When the impact failure strains were compared to that of the quasi-static loading, there was no clear dependency between the failure strain and applied strain rate. Because U1 samples have fibers aligned parallel to the loading direction, this observation suggests that the failure strain of the current carbon fibers is insensitive to the strain rate, at least within the range of strain rates that were tested.

An identical impact test procedure was applied to impact specimen U2. The strain versus time data for the specimen U2 impact test is shown in Fig. 9. The matrix-dominated specimens produced notable fluctuations in the longitudinal strain readings, potentially due to the propagation of stress waves in the fiber and matrix material during impact. These fluctuations were not observed in the fiber-dominated specimens. The strain versus time curves in Fig. 9 shows a distinct nonlinear strain response at strain values less than approximately 0.002 m/m while this initial nonlinearity was not observed in the fiber-dominated specimens. This characteristic was observed in all U2 samples. The most linear region of each curve in Fig. 9 was used to calculate a linear curve fit for the representative strain rate. Again, the failure strain was taken to be the point in each data set that strain readings diverged significantly from linearity.

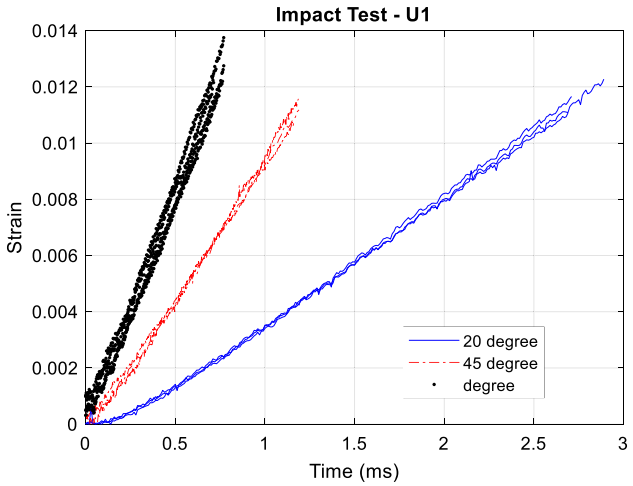

Fig. 8 Strain time-history of specimen U1 for three different impact angles

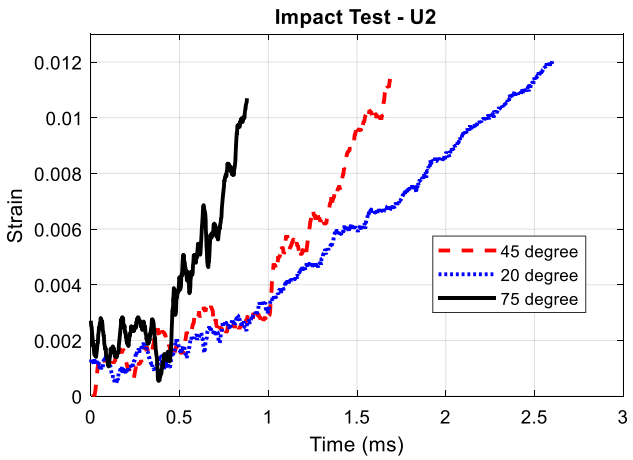

Fig. 9 Strain time-history of specimen U2 for three different impact angles

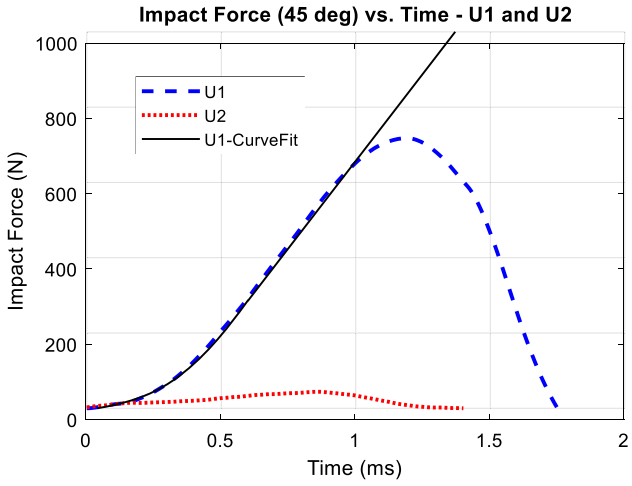

Fig. 10 Impact force time histories plots for specimens U1 and U2

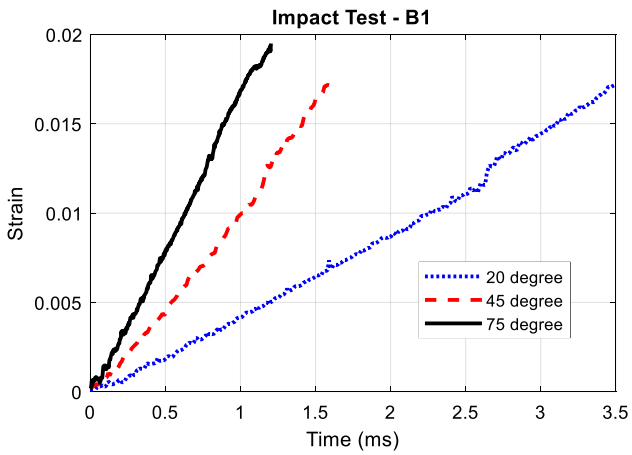

Fig. 11 Strain time history for impact specimen B1

The U2 specimens showed vastly different failure strains under Charpy impact tests as compared to that of the quasi-static loading test, while the failure strains were not much different among the three different impact angles. This is because the three different angles resulted in strain rates between 5 and 17 s^{-1}, which are much closer to one another as compared to the quasi-static strain rate of 2.8×10^{-4} s^{-1}. The impact force–time history was obtained for specimens U1 and U2, respectively. Figure 10 shows the impact forces. The plots resemble a half sine curve.

For specimen B1, strain rate test results at impact hammer angles of 20°, 45°, and 75° are shown in Fig. 11. The strain rate results of specimen B1 produced higher overall failure strains when compared to specimen U1. Additionally, the specimen B1 test duration at each impact hammer angle was slightly longer when compared to that of the unidirectional, fiber-dominated impact tests. At the largest impact angle of 75°, bidirectional specimen B1 produced an increase in failure strain with nearly 0.006 m/m when compared to the unidirectional specimen U1.

For specimen B2, strain rate test results at impact angles of 20°, 45°, and 75° are shown in Fig. 12. The bidirectional specimen B2 produced failure strains that were, in general, greater than the bidirectional specimen B1. One of the 20° impact angle tests on specimen B2 displayed fluctuations in strain readings that were similar to those of unidirectional specimen U2. Again, strain rates for each specimen B2 impact test were calculated using linear curve fitting.

The orthogonal orientation of the bidirectional impact specimens appeared to have a diminished effect on the strain rate behavior when compared to the unidirectional impact specimens. The difference between specimens B1 and B2 is that 1/3 of the total layers is either fiber-dominated or matrix-dominated. This is in contrast to the unidirectional impact specimens, in which every composite layer is fiber-dominated or matrix-dominated, respectively. Similar to the

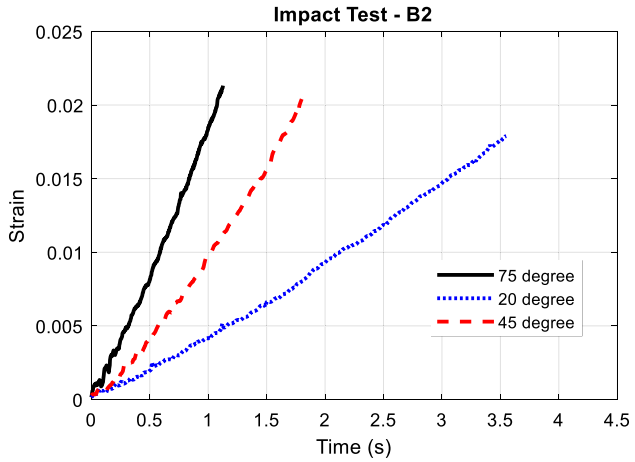

Fig. 12 Strain time history for impact specimen B2

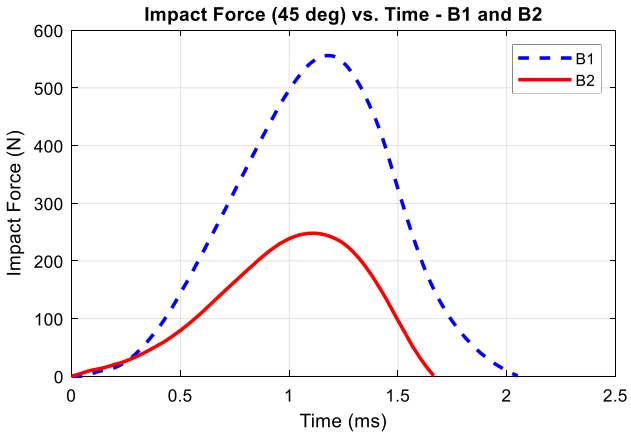

Fig. 14 Impact force time histories of specimens B1 and B2

results of unidirectional impact specimens U1 and U2, the impact specimens B1 and B2 produced strain rates and failure strains that were similar in magnitude. Figure 13 displays a comparison of the failure strain and supplied strain rate for all impact specimens.

As shown in Fig. 13, the failure strains of the bidirectional specimens B2 are relatively close in magnitude at each of the three impact hammer angles. At the highest impact angle of 75°, specimen B2 produced a mean strain rate that was greater by nearly 2 s^{-1} than specimen B1 at the same impact angle. The strain rate values at two other impact angles differed slightly between specimens B1 and B2.

Figure 14 shows the impact loading time history for the specimens B1 and B2. The peak impact load for specimen B1 is about two times greater than that for specimen B2. This is because specimen B1 has more 0° layers along the specimen length which are also at the outer layers of the specimen. The time duration of the impact force is slightly longer for specimen B1 than specimen B2.

6 Numerical results and discussion

With respect to the failure criteria described in the previous section, Eqs. (3)–(5) and (8)–(10) were used in the numerical model to predict the failure of the composite specimens to validate the proposed strain rate-dependent failure criteria.

First, quasi-static tensile specimens were simulated using the static finite element models while impact test models were analyzed using time-dependent dynamic analyses. Strain data were obtained from the finite element models that corresponded with the locations of the applied strain gage on the experimental specimens. The numerical tensile specimens were stretched uniformly in an incremental manner along the longitudinal direction until the specimen indicted failure.

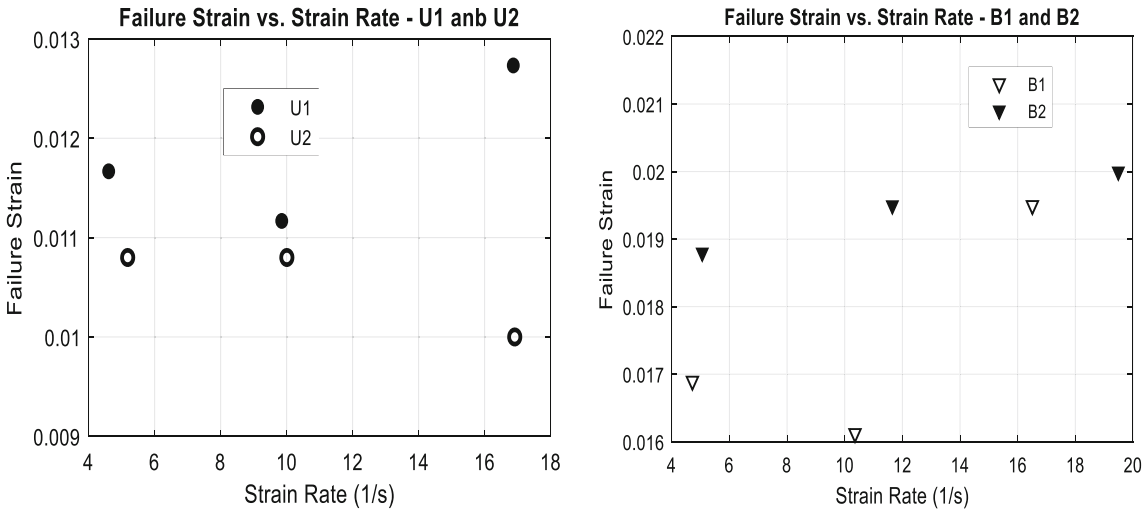

Fig. 13 Plots of failure strain versus strain rate for impact specimens

Table 4 Comparison of failure strains

	U1	U2	B1	B2
Experimental stress	1380 MPa	51.4 MPa	1120 MPa	477 MPa
Numerical stress	1310 MPa	50.4 MPa	901 MPa	495 MPa
Error	− 5.1%	− 1.9%	− 19.6%	3.8%
Experimental strain	0.0117	0.0066	0.0123	0.0109
Numerical strain	0.0117	0.0066	0.0117	0.0117
Error	0.0%	0.0%	− 4.9%	7.3%

Table 4 compares the failure stresses and strains between the experimental and numerical results for the quasi-static specimens. The experimental data are the average of two test results for each case. Failure stress and strain errors for specimen U1 were − 5% and 0%, respectively. Likewise, those values for specimen U2 were − 2% and 0%, respectively.

The numerically predicted failure strain for specimen B1 under-predicted the experimental failure strain by about 5% while the numerical failure stress under-predicted the experimental counterpart by almost 20%. When comparing specimens U1, B1, and B2, the number of longitudinal layers is six, four, and two for those specimens, respectively. This suggests that the failure stress should be approximately proportional to the number of longitudinal layers because the longitudinal layers are the major load-carrying layers. In that perspective, specimen B1 had higher failure stress than expected. One possible reason is the quasi-static specimen B1 might have higher fiber volume fractions (per layer) than the other samples. Because a unidirectional composite plate does not necessarily have a uniform fiber distribution inside the plate, some specimens cut out of the location with a higher fiber volume fraction become stronger.

The numerical results of specimen B2 over-predicted the experimental stress by 4% and strain by 7%. Overall, the prediction of the quasi-static failure stresses and strains of various composite specimens was reliable when the numerical and experimental results were compared.

The experimentally measured impact force–time history for the 45 impact angle, as shown in Figs. 10 and 14, was applied to the respective impact model. Figure 15 shows a typical longitudinal strain plot of an impact model at any instant. The strain at the center of the tensile surface was collected as a function of time until the numerical specimen failed.

The numerical and experimental strains are compared in Fig. 16 for the impact specimen U1. The results in Fig. 16 show a correlation between the experimental and simulated strain data. Multiple experimental data were plotted in the figure to show the repeatability of the measured strains. The initial 0.4 ms of the finite element strain curve is nonlinear. This is considered to be a result of the load curve used in Fig. 10. The impact force is nonlinear until approximately 0.4 ms. The linear portion of the numerical result of the

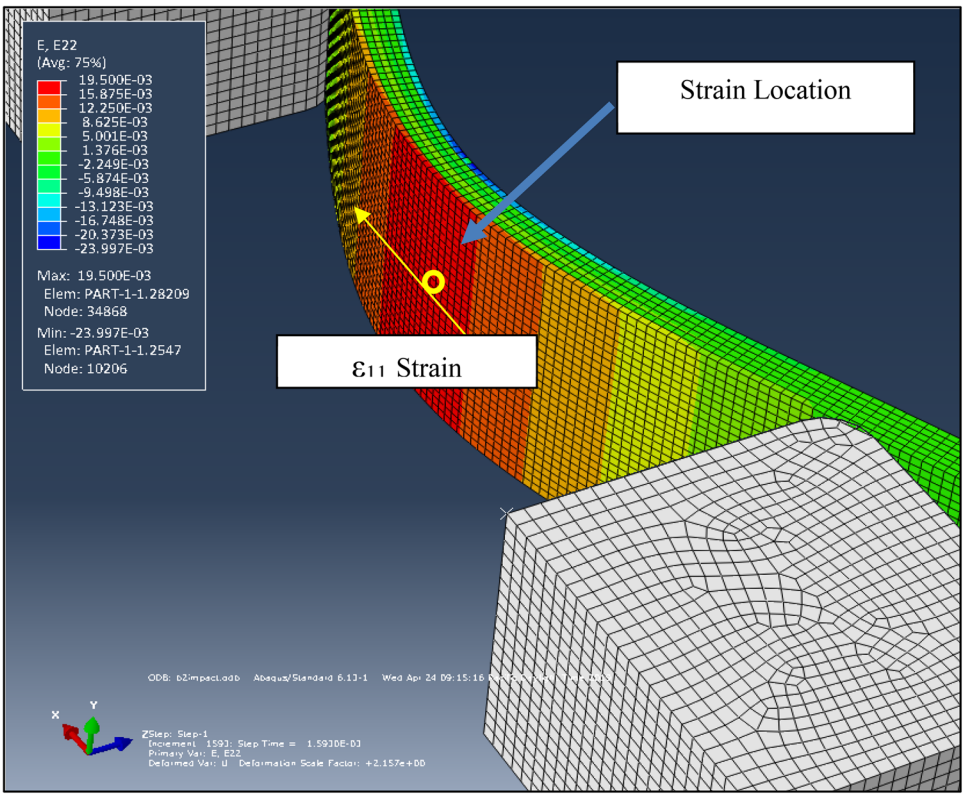

Fig. 15 A typical longitudinal strain plot for an impact specimen

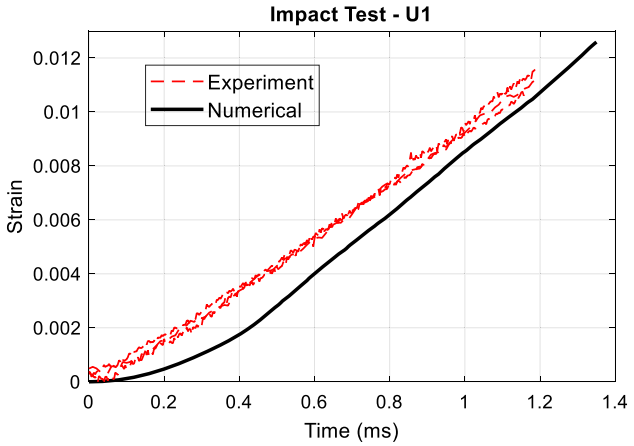

Fig. 16 Comparison of strain time histories for impact specimen U1

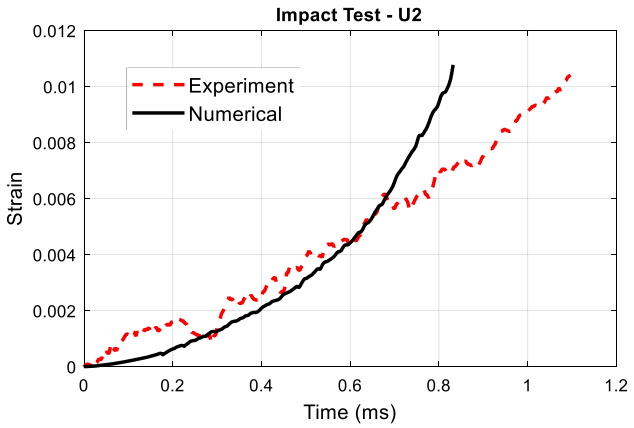

Fig. 17 Comparison of strain time histories for impact specimen U2

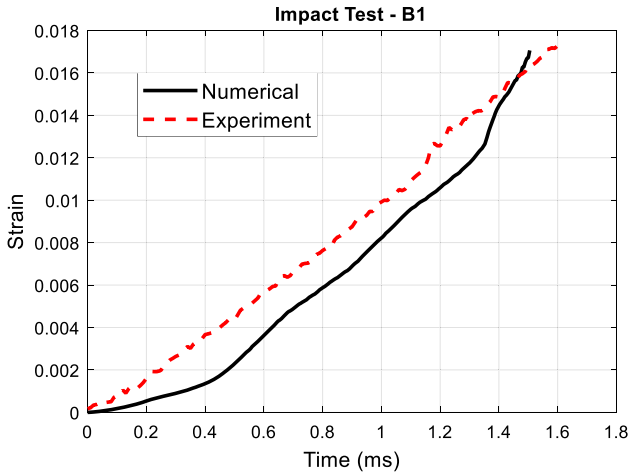

Fig. 18 Comparison of strain time histories for impact specimen B1

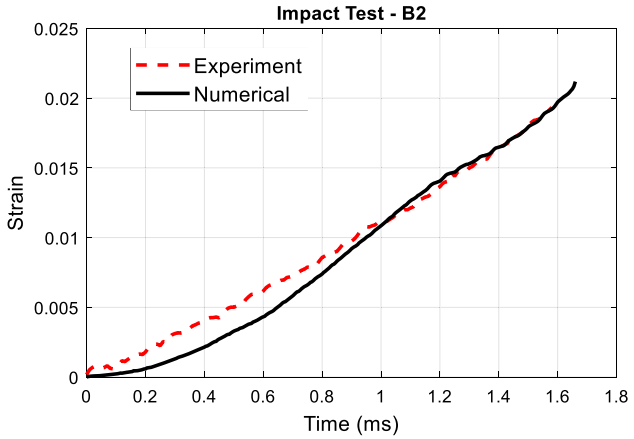

Fig. 19 Comparison of strain time histories for impact specimen B2

impact specimen U1 produced a strain rate of approximately 10.07 s^{-1}; compared to the experimental 45° impact hammer strain rate of 9.85 s^{-1}. The difference in the strain rate was approximately 2%. The numerical model for specimen U1 predicted a failure strain of approximately 0.0125 m/m as compared to the experimental failure strain of 0.0115 m/m. The error was 8.7%.

Figure 17 shows the comparison of the experimental and numerical results for the impact specimen U2. Both strain—time plots agreed well until around 6 ms. Then, the numerical strain showed failure at an earlier time. However, the failure strain agreed very well between the two results. The predicted failure strain was 3.8% greater than the experimental value.

The experimental data for impact specimen B1 are plotted in conjunction with the finite element data in Fig. 18. The finite element result generated by specimen B1 experienced the same initial nonlinearity as specimen U1, as explained. The finite element model produced a slight increase in strain rate during the final 0.2 ms of the simulated impact. This is indicative of fiber-dominated layer failure. The numerical specimen B1 for the impact model produced a linearized strain rate of approximately 10.90 s^{-1} between 0.5 ms and 1.3 ms, which was 5.2% greater than the experimental mean strain rate of 10.36 s^{-1}. Additionally, the failure strain of specimen B1 was 0.0171 m/m from the numerical model and 0.0175 m/m from the experimental result. The difference was − 2.3%.

Figure 19 compares the experimental and numerical strain plots for the impact specimen B2. Visual inspection of Fig. 19 indicated that there is a good agreement between simulated and experimental results. Curve fitting the numerical model gave the strain rate of approximately 13.50 s^{-1}; compared to the experimental value of 12.50 s^{-1}. This is about an 8.0% difference. The numerical failure strain for specimen B2 was approximately 0.0208 m/m, which is slightly greater than the experimental mean failure strain of 0.0195 m/m. The error was 6.7%.

The last example of numerical analysis was an AS4/3501-6 carbon/epoxy composite reported in Daniel et al. (2017). The composite plate was subjected to the combined transverse normal and shear stresses. The composite was tested at

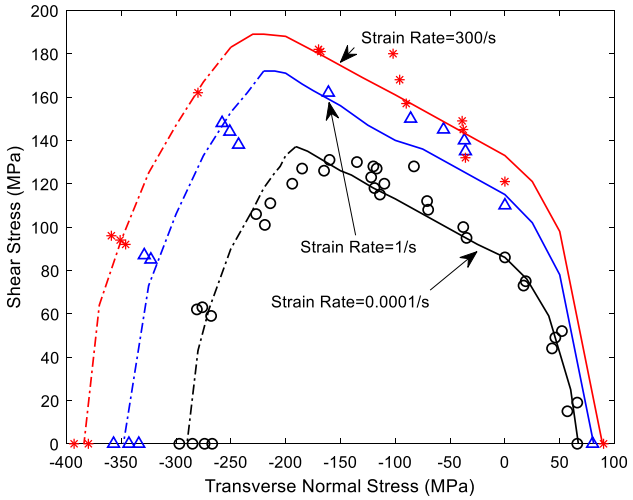

Fig. 20 Comparison of the experimental and numerical results for AS4/3501-6 carbon/epoxy composite

three different strain rates; $\dot{\varepsilon} = 10^{-4}$ s^{-1}, $\dot{\varepsilon} = 1$ s^{-1}, and $\dot{\varepsilon} =$ 200–400 s^{-1}. To validate the present failure criteria, the same strain rates as tested were used: $\dot{\varepsilon} = 10^{-4}$ s^{-1}, $\dot{\varepsilon} = 1$ s^{-1}, and $\dot{\varepsilon} = 300$ s^{-1}. The last one used the average strain rate of the test data. For the study $\alpha = 0.05$ and $\dot{\varepsilon}_o = 10^{-4}$ s^{-1} were selected for Eq. (7), and the comparison of the failure envelops between the experimental and the numerical results is shown in Fig. 20. The test data are denoted by symbols while the analytical results are represented by lines. Solid lines indicate the fiber/matrix interface failure, and the broken lines indicate the matrix failure. Therefore, each failure envelop consists of two failure modes. The comparison is very reasonable.

7 Conclusions

A previously developed set of failure criteria based on a multiscale technique was modified to implement the strain rate effect. Because the failure criteria distinguished failure modes in terms of fiber and matrix materials discretely as well as fiber/matrix interface failure, the strain rate property of each constituent material, like the fiber and matrix, can be implemented directly into the failure criteria. For the polymer composite materials studied here, the fiber material was insensitive to the strain rate while the matrix material was sensitive to the strain rate. As a result, the fiber failure criterion did not include the effect of the strain rate while the matrix and fiber/matrix interface failure criteria included the strain rate effect.

To validate the proposed strain rate-dependent failure criteria, both quasi-static and dynamic impact tests were conducted, respectively, for various specimens such as unidirectional and cross-ply laminates. The experimental results were compared to the numerical predictions obtained using the present failure criteria. Additional numerical analyses were conducted for another set of carbon composites in the literature. Overall, the present criteria compared well with the experimental results in terms of the failure strain and failure time including the strain rate effect.

Acknowledgements Dr. Chanman Park provided technical supports for the experimental testing. This work was supported by Office of Naval Research (ONR), and the Program Manager is Dr. Yapa Rajapakse.

Compliance with ethical standards

Conflict of interest The authors declare that they have no conflict of interest.

References

Abaqus 6.13 User Manual (2015) Dassault Systemes Inc
Daniel IM, Werner BT, Fenner JS (2011) Strain-rate-dependent failure criteria for composites. Compos Sci Technol 71(3):357–364
Daniel IM, Daniel SM, Fenner JS (2017) A new yield and failure theory for composite materials under static and dynamic loading. Rajapakse YDS (ed) Marine composites and sandwich structures. Office of Naval Research Solid Mechanics Program, pp 217–226
Hashin Z (1980) Failure criteria for unidirectional fiber composites. J Appl Mech 47(2):329–334
Hinton M, Kaddour A, Soden P (eds) (2004) Failure criteria in fibre reinforced polymer composites: the world-wide failure exercise. Elsevier, Amsterdam
Hsiao HM, Daniel IM (1998) Strain rate behavior of composite materials. Compos Part B Eng 29(5):521
Hütter U, Schelling H, Krauss H (1974) An experimental study to determine failure envelope of composite materials with tubular specimens under combined loads and comparison between several classical criteria. In: NATO AGARD conference proceedings, vol 163, pp 3.1–3.11
Jacob GC, Starbuck JM, Fellers JF, Boeman RG (2004) Strain Rate effects on the mechanical properties of polymer composite materials. J Appl Polym Sci 94(1):296–301
Kwon YW (2016) Multiphysics and multiscale modeling: techniques and applications. CRC Press, Boca Raton
Kwon YW, Darcy J (2018a) Failure criteria for fibrous composites based on multiscale modeling. Multiscale Multidiscip Model Exp Des 1(1):3–17
Kwon YW, Darcy J (2018b) Further discussion on newly developed failure criteria for fibrous composites. Multiscale Multidiscipl Model Exp Des 1(4):307–316
Kwon YW, Kim C (1998) micromechanical model for thermal analysis of particulate and fibrous composites. J Therm Stress 21:21–39
Kwon YW, Park MS (2013) Versatile micromechanics model for multiscale analysis of composite structures. Appl Compos Mater 20(4):673–692
Kwon YW, Ponshock T, Molitoris JD (2016) Failure loading of metallic and composite cylinders under internal pressure loading. ASME J Press Vessel Technol 138(6):060909
Park MS, Kwon YW (2013) Elastoplastic micromechanics model for multiscale analysis of metal matrix composite structures. Comput Struct 123:28–38

Sierakowski RL (1997) Strain rate effects in composites. Appl Mech Rev 50(12):741–759

Sun C, Quinn B, Tao J, Oplinger D (1996) Comparative evaluation of failure analysis methods for composite laminates. Purdue University, School of Aeronautics and Astronautics, DOT/FAA/AR-95/109

Swanson S, Messick M, Tian Z (1987) Failure of carbon/epoxy lamina under combined stress. J Compos Mater 21(7):620–629

Tsai SW, Wu EM (1971) A general theory of strength for anisotropic materials. J Compos Mater 5(1):58–80